# Large-eddy simulation of dense gas dispersion over a simplified urban area

E. M. M. Wingstedt[a,b,*], A. N. Osnes[b,c], E. Åkervik[a], D. Eriksson[a,d], B. A. Pettersson Reif[a,c]

[a] *Norwegian Defence Research Establishment (FFI), Kjeller, Norway*
[b] *Department of Mathematics, University of Oslo, Oslo, Norway*
[c] *UNIK - University graduate center, University of Oslo, Kjeller, Norway*
[d] *Swedish Defence Research Agency (FOI), Umeå, Sweden*

---

## Abstract

Dispersion of neutral and dense gas over a simplified urban area, comprising four cubes, has been investigated by the means of large-eddy simulations (LES). The results have been compared to wind tunnel experiments and both mean and fluctuating quantities of velocity and concentration are in very good agreement.

High-quality inflow profiles are necessary to achieve physically realistic LES results. In this study, profiles matching the atmospheric boundary layer flow in the wind tunnel, are generated by means of a separate precursor simulation.

Emission of dense gas dramatically alters the flow in the near source region and introduces an upstream dispersion. The resulting dispersion patterns of neutral and dense gas differ significantly, where the plume in the latter case is wider and shallower. The dense gas is highly affected by the cube array, which seems to act as a barrier, effectively deflecting the plume. This leads to higher concentrations outside of the array than inside. On the contrary, the neutral gas plume has a Gaussian-type shape, with highest concentrations along the centreline.

It is found that the dense gas reduces the vertical and spanwise turbulent momentum transport and, as a consequence, the turbulence kinetic energy. The reduction coincides with the area where the gradient Richardson number exceeds its critical value, i.e. where the flow may be characterized as stably stratified. Interestingly, this region does not correspond to where the concentration of dense gas is the highest (close to the ground), as this is also where the largest velocity gradients are to be found. Instead there is a layer in the middle of the dense gas cloud where buoyancy is dynamically dominant.

*Keywords:* LES, Wind tunnel, Dispersion, Dense gas, Urban flow, Atmospheric boundary layer

---

## 1. Introduction

Release and aerial dispersion of toxic industrial chemicals (TIC) may threaten the lives and health of an urban population and adversely affect the environment. To identify effective countermeasures, responsible authorities would benefit from having reliable estimates of the spatial and temporal evolution of the averaged and instantaneous concentration levels of the toxic cloud. Extensive research and development efforts are currently directed towards improving the reliability of simulation tools used to predict urban dispersion, in particular for neutral gases, i.e. gases with the same density as air. Significant progress have been made, and the most advanced tools based on computational fluid dynamics (CFD) approach have been demonstrated to reliably predict the transport and dispersion of neutral gases in complex urban environments (cf. e.g. [1, 2, 3, 4]). Urban dispersion and transport of non-neutral TICs, i.e., denser-than-air or lighter-than-air gases, however, still pose severe challenges and remains, from an operational point of view, largely unsolved.

Urban dispersion and transport usually takes place in complex built-up areas. While being driven by the large-scale atmospheric wind field, the dispersion and transport within an urban environment occur on scales comparable to the thickness of the atmospheric boundary layer, i.e. in the order of hundreds to a thousand meter. Hence, it becomes necessary to consider geometrical variations within the area of interest that are of the same order of magnitude as the distance over which the TIC is transported; the urban wind field is therefore inherently linked to the basic topography, the layout of buildings and streets, and even the occurrence of vegetation such as trees and bushes in parks and along streets. It should be noted that even if the wind field within the urban environment is primarily governed by the blocking effects of buildings, the incoming atmospheric boundary layer still plays a crucial role for the transport and mixing processes, in particular above the buildings.

From a modelling perspective, the transport and dispersion of plumes consisting of gases and/or aerosols in the atmosphere are governed by the fundamental conservation laws of mass, momentum, and energy. Neutral gases are

---

[*] Corresponding author. FFI, P O Box 25, NO-2027 Kjeller, Norway

*Email address:* `emma-my-maria.wingstedt@ffi.no` (E. M. M. Wingstedt) transported with the wind field. This is most often the case also for non-neutral gases, however, due to e.g. density difference between the gas and the surrounding air both the turbulence field and the averaged wind field may be severely altered, and thereby also the mixing process. Consequently there exists a two-way coupling between a non-neutral plume and the wind field, which is absent for neutral plumes. Hence, the complexity of urban dispersion and transport increases significantly when considering non-neutral gas releases, and it is this effect that makes non-neutral releases so challenging.

Several studies regarding numerical simulation of dense-gas dispersion using the unsteady Reynolds-averaged Navier-Stokes (URANS) approach have been carried out in the past [5, 6, 7, 8] with fairly good results. The URANS method inherently assumes that the mean flow field is statistically unsteady, an assumption that is rather well suited for flows involving bluff body shedding which occurs downstream of building structures. Perhaps an even more commonly used CFD approach is the simpler statistically steady RANS approach (see e.g., [9, 10, 11, 12]). This method inherently excludes the unsteady large-scale shedding which in general results in an underprediction of the mixing of scalar fields.

The most physically appealing modelling approach that naturally includes the large-scale flow unsteadiness is large eddy simulation (LES). LES resolves the inherent unsteadiness of the three-dimensional large-scale turbulence irrespectively of the nature of the averaged flow field, in addition to any feature associated with statistically unsteady shedding. Previous studies using the LES approach for urban dispersion modelling of neutral gases have shown good results in predicting flow and concentration fields [2, 3, 4, 13]. However, the literature regarding LES for dense gas dispersion in urban-like geometries is scarce. The usefulness of LES can partly diminish because it depends more closely on the a priori unknown inflow boundary conditions than RANS-based methods. In order to minimize the effect of inappropriate inflow boundary conditions, excessively large computational domains or precursor simulations are often used. The drawback is that these methods generally increase the computational cost.

The present study utilizes state-of-the-art LES in combination with the use of recent wind-tunnel measurement data to study dense-gas dispersion over a simplified urban area. The objective of the study is two-fold: Firstly, to systematically study the differences between neutral and dense gas plumes approaching and interacting with a simplified urban-like geometry within an atmospheric turbulent boundary layer. Secondly, to address different methods to generate turbulent LES inflow data and to demonstrate the impact of the different choices on the downstream development of the boundary layer and their suitability in dispersion application.

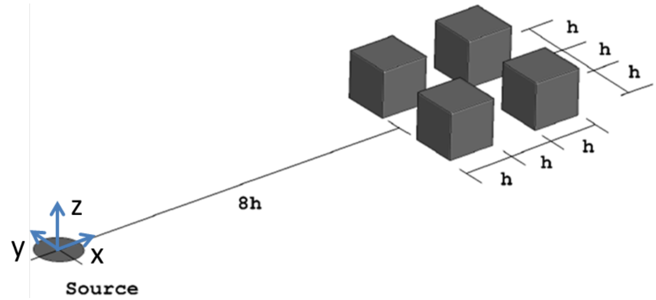

Figure 1: Schematic of the four cubes array in the wind tunnel. The cube dimension is $0.11 \times 0.11 \times 0.11$ m$^3$ and the source, with diameter $d = 0.1$ m, is located at the origin. The wall between the source and the cubes is smooth.

## 2. Experimental set-up

The domain of interest comprises four cubes aligned in a 2×2 array as shown in Figure 1. A low-vertical-momentum, circular source with diameter $d$ = 0.1 m is placed upstream the cubes. The cube dimensions are $h \times h \times h$ m$^3$, where $h$ = 0.11 m, whereas the incoming boundary-layer thickness, $H$, is approximately 1 m. Experiments were performed in the Environmental Flow Research Center's (EnFlo) meteorological wind tunnel at the University of Surrey, which is designed to study flow and dispersion processes within the atmospheric boundary layer. The low-speed, open-circuit wind tunnel has a test section of $20 \times 3.5 \times 1.5$ m$^3$ in the streamwise, spanwise, and wall normal directions, respectively. The thick incoming turbulent boundary layer was generated using vorticity generators at the inlet in combination with roughness elements placed on the ground. The boundary-layer characteristics are reported in Table 1 and the vertical profiles of mean streamwise velocity and Reynolds stresses are shown in Figure 4.

Table 1: Incoming boundary layer and source characteristics.

| Parameter | Description | |
|---|---|---|
| $H$ | Boundary layer thickness | 1 m |
| $U_\infty$ | Free-stream velocity | 1 m/s |
| $u_\tau$ | Friction velocity | 0.055 m/s |
| $h$ | Cube height | 0.11 m |
| $d$ | Source diameter | 0.1 m |
| $Q$ | Emission rate | 50 dm$^3$/min |
| $u_{emission}$ | Emission velocity | 0.1001 m/s |
| $\rho_{air}$ | Density of air | 1.1894 kg/m$^3$ |
| $\rho_{CO_2}$ | Density of $CO_2$ | 1.815 kg/m$^3$ |
| $\mu_{air}$ | Dyn. viscosity of air | 1.82 $10^{-5}$ kg/(ms) |
| $\mu_{CO_2}$ | Dyn. viscosity of $CO_2$ | 1.47 $10^{-5}$ kg/(ms) |

Velocity and turbulence measurements were conducted using a two-component Laser-Doppler Anemometer (LDA), whereas concentrations were measured using a

Fast Flame Ionisation Detector (FFID) with a frequency response of 200 Hz. Both the LDA and FFID systems have a positional accuracy of ±2 mm. FFID measures hydrocarbons. Therefore a small portion of propane, in order of 1%, was added to the emissions to act as a plume tracer. The emission consisted of air for the neutral release and carbon dioxide, which is approximately 1.5 times heavier than air, for the dense gas release. The cylindrical source installation, which extended below the wind tunnel floor, was packed with 3 mm beads and covered with a fine mesh in order to achieve a uniform emission. Details about the source and emissions can be found in Table 1, and details about the experiments can be found in [14].

## 3. Mathematical modelling

The filtered equations governing the conservation of mass and momentum of a Newtonian fluid with variable density are given by

$$\partial_t(\bar\rho) + \partial_j(\bar\rho\tilde u_j) = 0, \tag{1}$$

$$\begin{aligned}\partial_t(\bar\rho\tilde u_i) + \partial_j(\bar\rho\tilde u_i\tilde u_j) = {} & -\partial_i\bar p + \partial_j(2\bar\mu\tilde s_{ij}) \\ & + \bar\rho g_i - \partial_j\tau_{ij}.\end{aligned} \tag{2}$$

Here, the filtering operation is denoted by $\bar{(\cdot)}$ whereas $\tilde{(\cdot)}$ represents Favre (density-weighted) filtering. Favre filtering is introduced to cast the equations to a form where all unclosed terms are contained in a residual stress tensor and is defined as $\tilde{(\cdot)} = \overline{\rho(\cdot)}/\bar\rho$. Temporal and spatial gradients are denoted $\partial_t = \partial/\partial t$ and $\partial_i = \partial/\partial x_i = (\partial/\partial x, \partial/\partial y, \partial/\partial z)$, respectively. $\tilde u_i(\mathbf{x},t) = (\tilde u, \tilde v, \tilde w)$ and $\bar p(\mathbf{x},t)$ are the resolved velocity and pressure fields, respectively, and $g_i = (0,0,-g)$ is the gravitational acceleration. The variable density is defined as

$$\bar\rho(\tilde\zeta) = \frac{1}{\tilde\zeta\rho_{gas}^{-1} + (1-\tilde\zeta)\rho_{air}^{-1}}, \tag{3}$$

where $\tilde\zeta(\mathbf{x},t)$ is the mass fraction of gas in air. The dynamic viscosity, $\bar\mu(\tilde\zeta)$, is calculated in the same manner as $\bar\rho(\tilde\zeta)$. $\tilde s_{ij}(\mathbf{x},t)$ denotes the resolved strain-rate tensor given by

$$\tilde s_{ij} = \frac{1}{2}(\partial_j\tilde u_i + \partial_i\tilde u_j) - \frac{1}{3}\delta_{ij}\partial_k\tilde u_k. \tag{4}$$

It should be noted that $\tilde s_{ij}$ is trace free. The last term in (2) is the residual stress tensor, $\tau_{ij} = \bar\rho(\widetilde{u_iu_j} - \tilde u_i\tilde u_j)$, which is modelled using the Boussinesq assumption, i.e., $\tau_{ij} = -2\mu_t\tilde s_{ij}$. The eddy viscosity, $\mu_t(\mathbf{x},t)$, is modelled using the dynamic Smagorinsky approach. More details about LES theory and how to model the eddy-viscosity can be found in e.g. [15] and [16].

The filtered equation governing the transport of mass fraction of a scalar field is given by

$$\partial_t(\bar\rho\tilde\zeta) + \partial_j(\bar\rho\tilde\zeta\tilde u_j) = \partial_j\left(\bar\rho\alpha\partial_j\tilde\zeta\right) - \partial_j t_j, \tag{5}$$

where $\alpha$ is the scalar molecular diffusion coefficient. $t_j = \bar\rho(\widetilde{u_j\zeta} - \tilde u_j\tilde\zeta)$ represents the unresolved sub-grid scalar flux and is modelled similarly to the momentum sub-grid stresses, i.e., $t_j = -(\mu_t/Sc_t)\partial_j\tilde\zeta$, where the turbulent Schmidt number is $Sc_t = 0.9$. The exact value of $Sc_t$ is of minor importance here since the sub-grid terms are small, but in the literature common values lies between 0.1 – 1 [17]. The volume concentration of a released gas is calculated as (c.f. (3))

$$\tilde c(\tilde\zeta) = \frac{\tilde\zeta}{\rho_{gas}}\bar\rho(\tilde\zeta). \tag{6}$$

Note that the limiting behaviour $\tilde c(\tilde\zeta = 1) = 1$ corresponds to the condition at the source location.

The resolved flow fields can be decomposed into mean and fluctuating parts, i.e. $\tilde u_i = U_i + u_i$, $\bar p = P + p$, and $\tilde c = C + c$, where upper case letters represent the mean and lower case letters the fluctuations. All averages reported in Section 5 are averaged in time, e.g.

$$U_i(\mathbf{x}) = \langle\tilde u_i(\mathbf{x},t)\rangle = \frac{1}{T_{av}}\int_0^{T_{av}}\tilde u_i(\mathbf{x},t)\mathrm{d}t, \tag{7}$$

where $\langle\cdot\rangle$ denotes the averaging operator and $T_{av}$ is the averaging time. All root-mean-square variables, denoted with the subscript $rms$, are defined as the square root of the auto-correlation of that variable, e.g. $c_{rms} = \sqrt{c^2}$.

### *3.1. Numerical modelling*

The numerical simulations are performed using the low-Mach number, variable-density solver VIDA from Cascade Technologies. This is an unstructured, finite-volume based solver with a low-dissipation numerical scheme. A second order central differencing scheme for the momentum and a first order upwind scheme for the scalar field is employed. For more details the reader is referred to e.g. [18, 19, 20, 21].

In the present study, the floor and cubes are prescribed no-slip velocity boundary conditions. At the top and side walls of the wind tunnel, thin boundary layers will develop. These are believed to be of minor importance in this case, hence justifying the use of slip conditions at these locations. It is very important to prescribe appropriate turbulent inflow conditions when using LES methods. This will be discussed in more detail in Section 4. The computational domain, illustrated in Figure 2, is divided into approximately $6\cdot10^6$ hexahedral cells, where the cell density is highest around the source and the cubes. Characteristics of the computational resolution are summarized in Table 2.

Table 2: Grid sizes $(\Delta x, \Delta y, \Delta z)$ in the different regions of the computational domain. The size of the domain in the different directions are given by $L_x$, $L_y$, and $L_z$, respectively. In terms of viscous scaling, and based on the inflow velocity field, the coarsest resolution $\Delta x/h = 0.45$ within the entire computational domain corresponds to $\Delta x/l^+ = 185$.

| Region | $L_x/h$ | $L_y/h$ | $L_z/h$ | $\Delta x/h$ | $\Delta y/h$ | $\Delta z_{min}/h$ | $\Delta z_{max}/h$ |
|---|---|---|---|---|---|---|---|
| *Source* | | | | 0.015 | 0.015 | 0.001 | |
| $R_1$ | 19.4 | 6.1 | 2.1 | 0.05 | 0.05 | 0.01 | 0.05 |
| $R_2$ | 25.8 | 20.2 | 5.2 | 0.15 | 0.15 | 0.03 | 0.15 |
| $R_3$ | 45.5 | 32.1 | 13.7 | 0.45 | 0.45 | 0.09 | 0.45 |

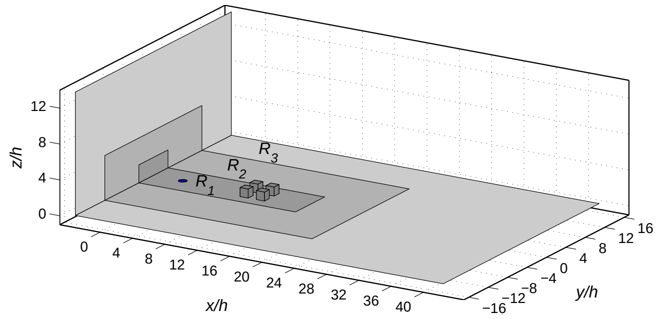

Figure 2: Illustration of the computational domain (c.f. also Figure 1). The region marked $R_1$ has the most dense grid resolution, whereas the region marked $R_3$ has the coarsest. Additional refinement is employed around the source location. The resolution of each region is found in Table 2.

## 4. Generation of inflow boundary condition

In order to achieve physically realistic LES results special care of the inflow boundary conditions needs to be taken. Several methods exist to generate such flow fields. The most straigthforward method is to generate boundary conditions from periodic precursor simulations (i.e. channel flow) [22, 23]. A generalization of this method, to account for spatial development, is provided by recycling methods where velocities at a selected downstream location are extracted, rescaled, and fed in as inflow at each time step [24, 25, 26]. In cases where sufficient data from experiments are available (for instance in the form of particle image velocimetry snapshots together with hotwire time series), it is possible to reconstruct velocity fields for inflow purposes directly from measurements [27, 28, 29]. For more general situations, where less experimental data are available and the flow is far from periodic, synthetic turbulence methods [30, 31, 32, 33, 34, 35, 36, 37] may be preferrable.

Here, the goal is to reproduce the boundary layer from the experiments described in Section 2, by means of separate precursor simulations, to be used as inflow for the dispersion simulations. In the wind tunnel, the flow is subject to the combined effects of the turbulent air produced by the fan, the vortex generators, and the obstacles on the floor. In order to examine the "minimal" modelling effort needed to reproduce the boundary layer flow, three different configuration are considered numerically:

(i) Synthetic turbulence inflow over a smooth wall,

(ii) synthetic turbulence inflow over a rough wall,

(iii) steady inflow (mean flow from the experiments) over a rough wall.

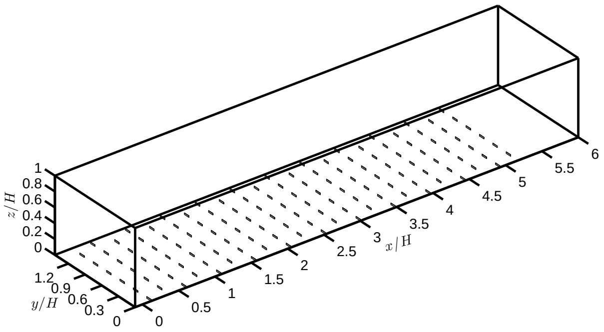

Figure 3: Illustration of part of the computational domain for the precursor simulations, with roughness elements and their relative placement corresponding to the wind tunnel set-up.

The synthetic turbulence method employed in the current work is similar to the one proposed in [36]. At each time step, random white noise is manipulated such that the two-point correlations and Reynolds stresses of the fluctuations match those given by the experiments. Subsequently the fluctuations are added to the mean flow. The roughness elements, consisting of thin plates of height $h_r = 0.02H$, are placed onto the floor in the region $0 < x/H < 5$ with a downstream spacing of $0.12H$. This configuration matches geometrically the set-up in the wind tunnel. Figure 3 illustrates the dimensions and placement of the obstacles. In all three simulations the computational domain size is $8H \times 1.44H \times 1.5H$ in the streamwise, spanwise, and wall-normal directions, respectively. A total of $13 \times 10^6$ computational cells, more than in the dispersion simulations, are used and the grid is subjected to a one-to-three splitting based on the distance to the wall. It should be noted that all three simulations use the same grid spacing, even though the smooth wall simulation could be well resolved with a coarser grid. Details about the grid resolution for the precursor simulations can be found in Table 3.

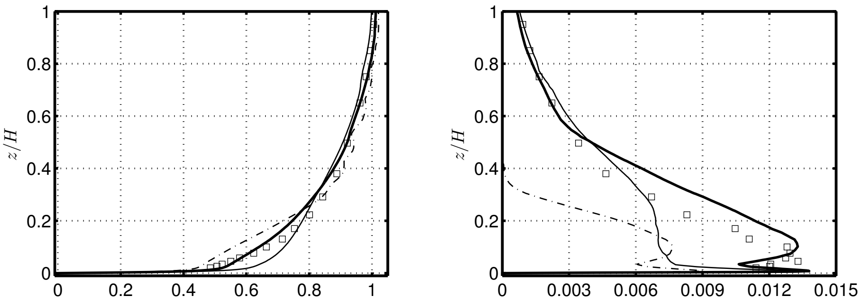

(a) Mean streamwise velocity $U/U_\infty$ (b) Streamwise Reynolds stress $\langle uu \rangle/U_\infty^2$.

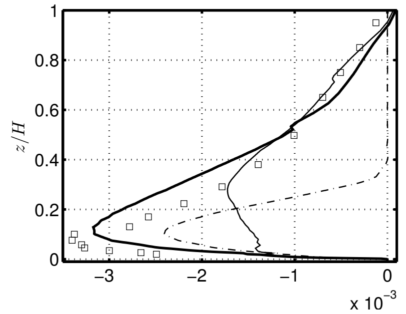

(c) Reynolds shear stress $\langle uw \rangle/U_\infty^2$.

Figure 4: Comparison of time- and spanwise-averaged vertical profiles from numerical simulations with experimental results. The simulation results are taken at the downstream position of $x/H = 6$. Recall that the roughness elements in the simulations span the length $x/H = 0$ to $x/H = 5$. Results from experiments (□), smooth wall with synthetic turbulence inflow (——), rough wall with synthetic turbulence inflow (——) and rough wall with steady inflow (− · −) are shown.

Table 3: Grid sizes based on distance from the wall in precursor simulations. In terms of viscous scaling, based on the friction velocity from the experiments, the resolution of $\Delta x/H = 0.004$ corresponds to 15 viscous units.

| $z/H$ | $\Delta x/H$ | $\Delta y/H$ | $\Delta z/H$ |
|---|---|---|---|
| 0 − 0.02 | 0.004 | 0.004 | 0.002 |
| 0.02 − 0.51 | 0.012 | 0.012 | 0.012 |
| 0.51 − 1.5 | 0.036 | 0.036 | 0.036 |

Vertical profiles of the mean streamwise velocity, streamwise Reynolds stress, and Reynolds shear stress are shown in Figures 4a-4c, respectively. The thin solid lines (——) represent synthetic turbulence inflow over a smooth wall (case i), the thick solid lines (——) represent synthetic turbulence inflow over a rough wall (case ii), and the dash-dotted lines (− · −) represent steady inflow over a rough wall (case iii). From Figure 4a it is seen that in the outer part of the boundary layer ($z/H > 0.3$), all three methods yield similar mean flow profiles, in close agreement with experiments. This indicates, as would be expected, that in the outer part of the boundary layer, advection by the mean flow is the dominant mechanism. Closer to the wall, case ii is clearly in better agreement with the experiments than the two others. While the roughness-produced boundary layer in case iii seems to have an almost constant velocity gradient below $z/H = 0.3$, the smooth-wall boundary layer in case i has a strong gradient close to the wall. In order to assess the quality of the smooth-wall simulation (case i), the friction velocity is compared to the flat-plate boundary-layer flow experiments of [38]. Indeed the friction velocity derived from the gradient of the mean flow (i.e. from the wall shear stress) at the wall, $u_\tau/U_\infty = \sqrt{\mu\rho^{-1}\partial_z U}/U_\infty = 0.036$, is in close agreement with [38]. Below $z/H \sim 0.02$, the mean flow, and therefore also the friction velocity, of case i and case ii are almost identical. In the experiments, the friction velocity is estimated as the square root of the mean Reynolds shear stress in the lower 20% of the boundary layer ($z/H < 0.2$), with a resulting value of $u_\tau/U_\infty = 0.055$. Figure 4c shows that only case ii has a shear stress magnitude comparable to the experiments. Indeed, using the Reynolds shear stress to define the friction velocity, it is found that $u_\tau/U_\infty = 0.037$ for case i, $u_\tau/U_\infty = 0.051$ for case ii, and $u_\tau/U_\infty = 0.044$ for case iii. Clearly case ii has the best agreement with the experiments. It is interesting to note that in case i the two ways of defining the characteristic velocity scale are almost identical indicating that there is a constant stress layer, as expected for a flat plate boundary layer flow. On the contrary, for the roughness boundary layer flows in case ii and case iii, the friction velocities based on wall shear stress are significantly lower than the ones based on Reynolds shear stress. Hence, the most important contribution to turbulent mixing stems from the pressure drag created by the upstream obstacles.

In terms of streamwise Reynolds stresses, case ii is in better agreement with experiments than the two others. Interestingly, the near-wall behaviour ($z/H < 0.02$) of case i and case ii is again very similar. Case i has a single peak in the streamwise Reynolds stress, located slightly below $z/H = 0.01$ (about 20 wall units). Case ii on the other hand, has a double peak behaviour, with the first peak being almost identical to case i, both in location and magnitude, and the second peak located at $z/H = 0.1$. The inner peak is related to viscous mechanisms, whereas the outer peak is related to turbulence produced by the aerodynamic drag of the obstacles. Case iii also has a double peak behaviour, with the peaks located approximately at the same locations as in case ii, but with significantly lower amplitude. In Figures 5b and 5a, snapshots of the instantaneous streamwise velocity for case ii and case iii are shown. The synthetic turbulence in case ii provides large-scale structures not present in case iii. From the snapshots it is not clear whether this has an impact on the near wall behaviour. On the other hand, the vertical profiles of the Reynolds stresses, shown in Figures 4b and 4c, confirms that this is the case. By inspection of the downstream development of the Reynolds stresses in case iii, it is found that the thickness of the turbulent region increases with increasing downstream distance from the inlet. However, this development is slow, and it is estimated that the array of obstacles would have had to be three times as long as for the case with synthetic turbulence in order to obtain Reynolds stress profiles that resembles the experiments.

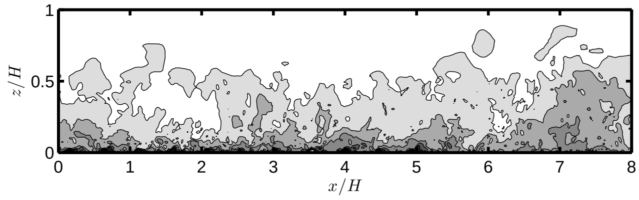

(a) Flow over rough wall with synthetic turbulence inflow (case ii).

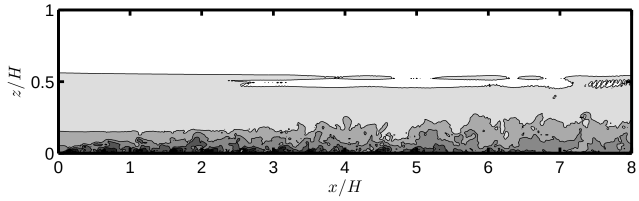

(b) Flow over rough wall with steady inflow (case iii).

Figure 5: Two-dimensional planes of normalized instantaneous streamwise velocity. Contour levels are $-0.2, 0, \ldots, 1.0$, where black corresponds to $-0.2$ and white corresponds to 1.0.

To conclude, the combination of roughness elements and synthetic turbulence is the appropriate way of providing sufficient quality inflow profiles for the dispersion simulations. It should be noted that the boundary layer flow could in principle be produced directly in the dispersion simulation, however, the results presented here, show that this is not a viable option for atmospheric dispersion simulations. Firstly, to produce a high quality boundary layer flow requires testing and validation. This testing is best facilitated in separate simulations. Secondly, the same background boundary layer flow is reused for different dispersion scenarios. In the present case, one neutral gas release and one dense gas release, but in general many more configurations may be investigated. Therefore, to include the inflow region in the dispersion simulations would be computationally costly.

## 5. Results

In this section results from the dispersion simulations are presented and discussed. Numerical results are compared to the experimental data along two vertical and two horizontal lines, which are taken at the centreline upstream the cubes ($x/h = 6.88$) and in-between the rows of cubes ($x/h = 9.5$). All lateral profiles have been mirrored about the symmetry line ($y = 0$) in order to improve the statistics.

### *5.1. Mean velocity field*

As already stated, it is crucial to be able to predict the velocity field in order to accurately foresee the dispersion. This section will validate the numerical results to experiments and describe the main features of the mean flow field.

Figure 6 shows the vertical variation of mean streamwise velocity, normalized by the free-stream velocity, predicted by the simulations as well as the experimental values. Already upstream of the cubes, a significant difference between the neutral and dense-gas case is visible; the velocity in the dense-gas case is higher below the cube height. Close to the ground, the velocity gradient is significantly lower in the dense gas case. In fact the wall shear stress is reduced by a factor of five. Between the cubes the difference is smaller but still noticeable. In both the neutral and dense gas case, the mean streamwise velocity is very well predicted.

Figure 7 shows a visualisation of the mean velocity field at height $z/h = 0.25$ using the line-integral convolution (LIC) technique [39]. With release of neutral gas (Figure 7a) the mean flow field is only weakly affected by the emission (i.e. the vertical momentum of the source) and the most important features of the flow field are generated by the cube array. The primary effect of the cube array is the deflection of the flow around the array. In front of the cubes, there are saddle points, located at $(x/h,\ y/h) \approx (7.0,\ \pm 0.75)$, where the flow separates and the incoming flow is deflected vertically and away from the centreline. From the saddle points, there are paths where

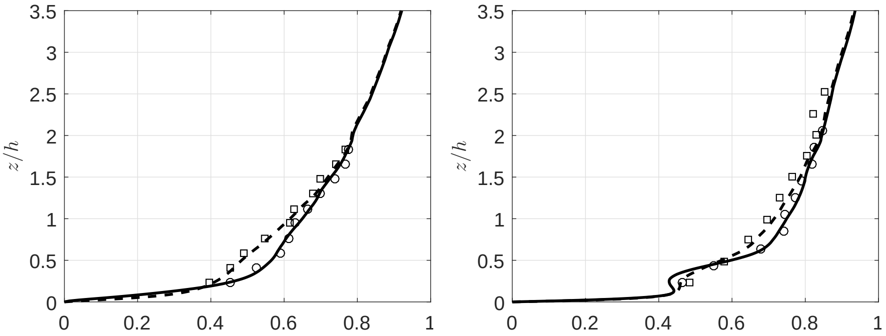

(a) $U/U_\infty$ at $x/h = 6.88$.

(b) $U/U_\infty$ at $x/h = 9.5$.

Figure 6: Vertical variation of normalized mean streamwise velocity of dense gas (——, ∘) and neutral gas (– –, □) at two different $x$-positions on the centreline. Lines show numerical results and symbols mark experimental values.

the streamlines converge, which is a signature of the outer edge of a flow region dominated by a pair of horseshoe vortices that wrap around the outside and in between the cubes.

Behind the last row of cubes, the presence of two arc-vortices, one behind each cube, is quite evident from the spiralling streamlines. These arc-vortices are located within the recirculation region which extend to $x/h \approx 12.3$. Behind the source there is evidence of a similar recirculation region as was seen behind the cubes, which ends roughly at $x/h \approx 1.5$.

The mean flow field at height $z/h = 0.25$ with the dense gas release is similar to the mean flow field for the neutral gas release close to the cubes in terms of flow features, but their locations are slightly shifted. However, there are significant differences in the wind field upwind of the cubes and also in the areas further away from the centreline. Here, the dense gas introduces a significant lateral motion, clearly visible in Figure 7b.

The flow field in the immediate proximity of the source is also very different in the neutral and dense cases, as emphasised by the insets in Figures 7a and 7b. In the dense gas case, there is a sequence of critical points along the centreline in the mean velocity field. The critical points, ordered from left to the right are a saddle point, unstable node, another saddle point and another unstable node, where the unstable nodes are the very visible dark areas in the inset. The first two critical points are signatures of a horseshoe vortex upstream of the source, and marks the boundary of the region where the flow is dominated by this vortex. The last two critical points are similarly signatures of another vortex downstream of the source, rotating in the same direction as the upstream vortex.

Figure 8 shows the mean velocity field in a vertical plane in the proximity of the source at $y/h = 0$ for both neutral and dense gas release. As seen from the LIC images, the sources affect the mean flow field differently and the difference can be attributed density effects. In the neutral case (Figure 8a) the streamlines from the source travel vertically and gradually turns and becomes horizontal lines. In studies of neutral jets in cross-flow, the jet is often characterized by the ratio of emission velocity to cross flow velocity, $u_{emission}/U_\infty$. Here, this ratio is 0.1, hence the source can be considered a low velocity ratio jet. The dynamics of these jets have been investigated, and are expected to be dominated by hairpin vortices [40]. For release of dense gases, a more suitable measure would be the ratio of jet momentum to boundary layer momentum. In this case using carbon dioxide the ratio is approximately 0.15, which corresponds to a low momentum source and the flow is expected to be dominated by the same kind of vortices.

The hairpin vortices are formed due to cancellation of the counter-clockwise vorticity on the upwind side of the source by the clockwise vorticity present in the incoming boundary layer. Hence, a hairpin vortex is formed instead of a complete vortex ring as would be expected for emissions with a high velocity ratio. In the dense gas case (Figure 8b) the streamlines starting from the source quickly turn downward and a vortex is clearly seen on the downstream side of the source. The upwind vortex discussed above can also be observed in this image. As seen from the figure, both the upwind and the downwind vortices are rotating clockwise, and can therefore not be part of a single vortex ring. This indicates that the source can still be considered as a low velocity-ratio source, but there are clearly additional effects introduced due to the density difference between the incoming flow and the emitted gas.

### *5.2. Concentration field*

Figures 9a and 9b show the vertical variation of mean concentrations of dense and neutral gas, respectively, at two locations. The concentrations are very well predicted compared to experimental data. Upstream of the cubes, the dense gas has high concentrations close to the ground and the gas is not transported above the cube height. Neutral gas, on the other hand, is more mixed and higher concentrations are found also above the building structures. In-between the cube rows, the maximum concentrations of both dense and neutral gas are reduced as compared to in front of the cubes.

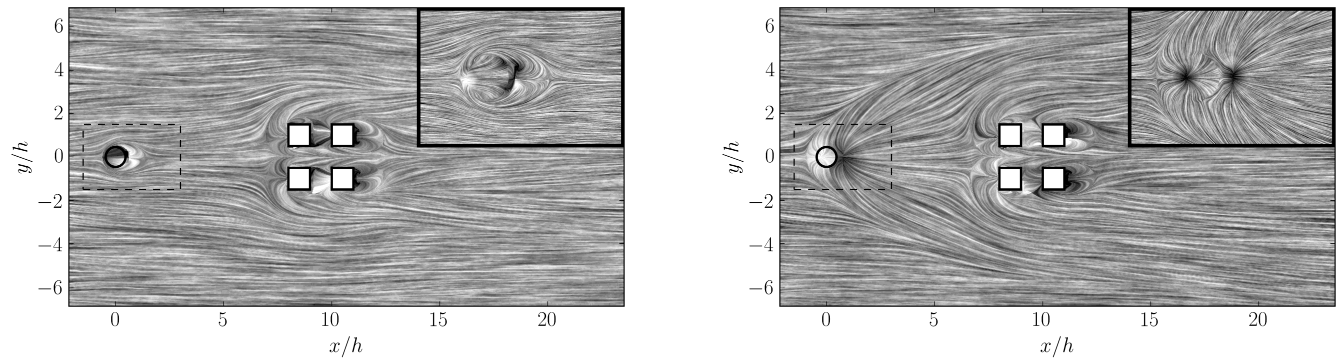

(a) Neutral release

(b) Dense gas release

Figure 7: Mean velocity field, predicted by the LES, at height $z/h = 0.25$ visualised using LIC. The insets show a close-up view of the flow fields around the sources as indicated by the dashed lines.

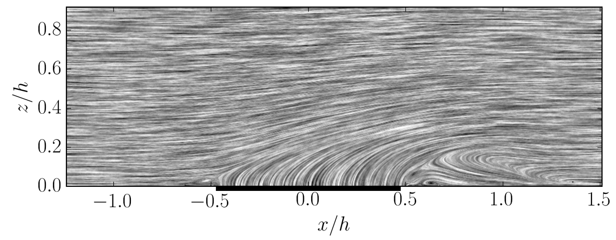

(a) Neutral release

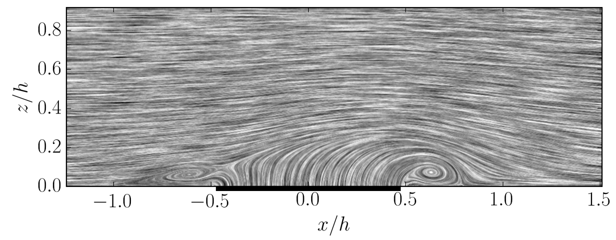

(b) Dense gas release

Figure 8: Mean velocity field, predicted by the LES, at $y = 0$ m visualised using LIC. The dark line below the $x$-axis shows the location of the source.

The concentration fluctuations (Figures 9c and 9d) show similar behaviour as the mean concentration with relatively high fluctuations close to the ground and almost no fluctuations above the cubes for the dense gas. The fluctuations of dense gas are smaller compared to the neutral gas, even in the region where the dense gas has a higher mean value. An interesting feature, most prominently seen upstream the cubes, is that there are areas where the fluctuations are larger than the mean value. This is especially true for the neutral gas, where the fluctuations are up to twice the value of the mean. Again, the simulated results correspond excellently to the experiment.

The lateral variation of mean concentration of neutral and dense gas at height $z/h = 0.25$ is seen in Figure 10. A slight asymmetry in the experimental values, particularly visible in Figure 10b, might indicate a deviation from the two-dimensionality in the wind tunnel inflow. The dense gas concentration is slightly overpredicted upstream of the cubes but the simulations manage to get the width of the plume correct. It should be noted that the dense gas concentration field varies greatly with height (steep gradient) close to the ground as seen in Figure 9a. Hence, a small deviation in measurement position in the experiments would lead to higher/lower concentration levels predicted by the simulations.

Between the cubes, the dense gas forms three peaks among which the concentration is slightly higher in the outer two. The three peaks are also seen in the experimental results, but here the concentration in the center peak is higher. However, this is probably due to the somewhat sparse measurement positions, and that the values have not been measured at the exact peaks.

The grey area included in Figure 10 shows all the values in between $C \pm c_{rms}$. The fact that $c_{rms}$ is higher than the averaged concentration shows that the time average may be less relevant. In the event of an actual release, a person could be exposed to a concentration far higher than the averaged value. Depending on the substance in question,

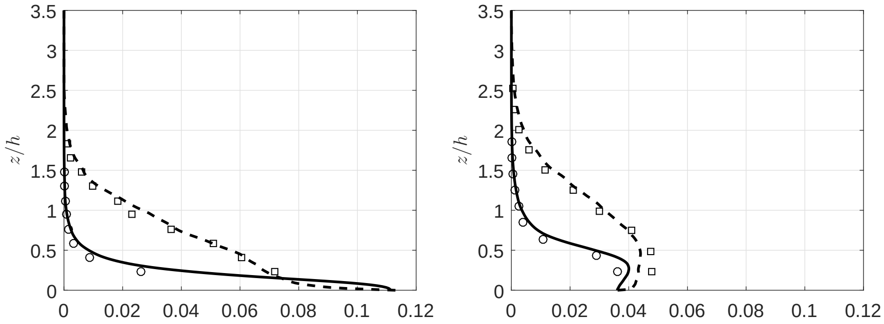

(a) $C$ at $x/h = 6.88$.

(b) $C$ at $x/h = 9.5$.

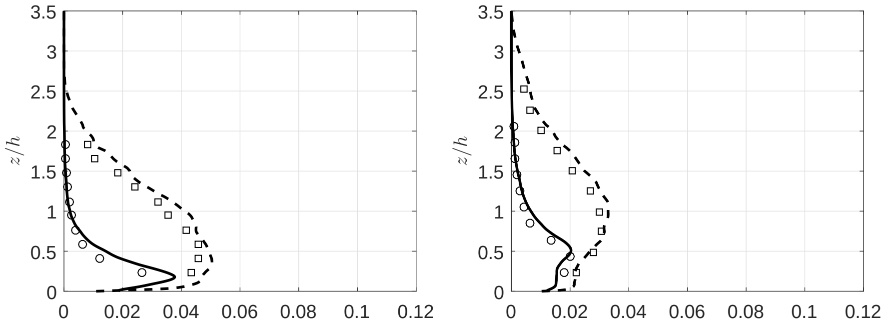

(c) $c_{rms}$ at $x/h = 6.88$.

(d) $c_{rms}$ at $x/h = 9.5$.

Figure 9: Vertical variation of mean concentration (a-b) and rms concentration (c-d) of dense gas (——, ○) and neutral gas (– – –, □) at two different $x$-positions on the centreline. Lines show numerical results and symbols mark experimental values.

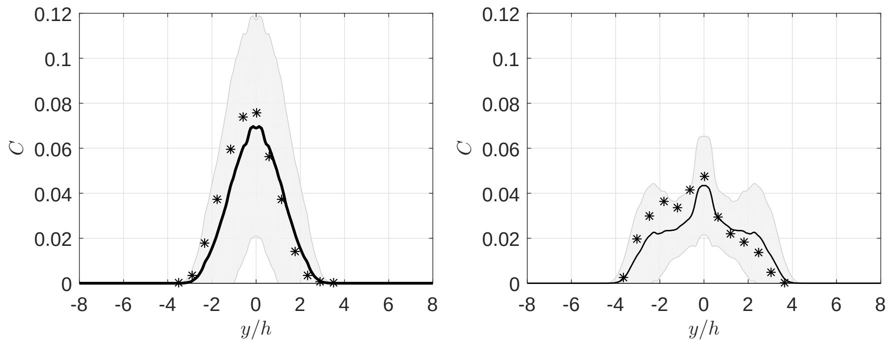

(a) $C$ of neutral gas at $x/h = 6.88$.

(b) $C$ of neutral gas at $x/h = 9.5$.

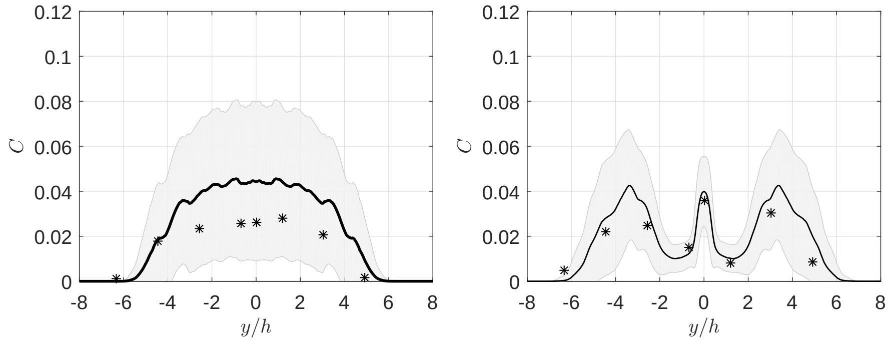

(c) $C$ of dense gas at $x/h = 6.88$.

(d) $C$ of dense gas at $x/h = 9.5$.

Figure 10: Lateral variation of mean concentration of neutral gas (a – b) and dense gas (c – d) at two different $x$-positions at height $z/h = 0.25$. Lines show numerical results and symbols mark experimental values. The grey areas show all values in between $C \pm c_{rms}$ predicted by the LES.

a short-duration exposure might be lethal and therefore a good prediction of the fluctuations is of great importance.

Figure 11 shows contours of the mean concentration for neutral and dense gas in a horizontal plane at height $z/h = 0.25$. The difference between the two fields is considerable. Where the bulk of the neutral gas travels toward the cube array, most of the dense gas plume spreads around it. This is most likely due to a combination of the difference in dispersion pattern from the source as well as the barrier that the cubes create for the dense gas cloud. Another interesting feature seen in Figure 11b is the higher concentrations right in front of the cubes compared to further upstream. This is again an effect from the cubes acting as a barrier against the dense gas.

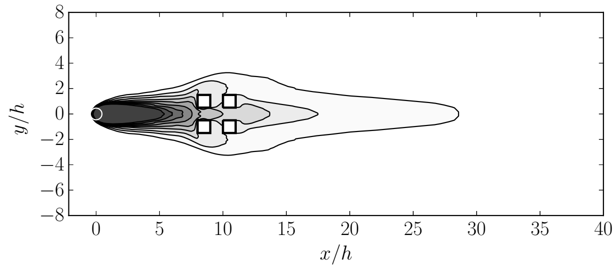

(a) Neutral gas

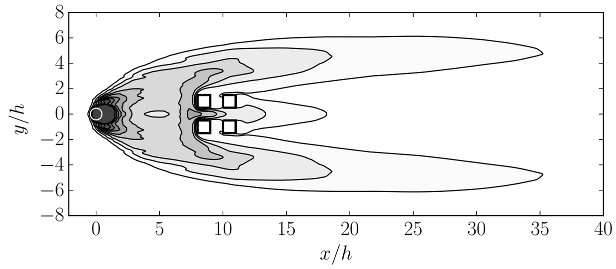

(b) Dense gas

Figure 11: Contours of the mean volume concentration of neutral and dense gas in a horizontal plane at height $z/h = 0.25$, with a contour spacing of 0.01. The white circles indicate the source locations and sizes.

Figure 12 shows contours of the mean concentration in vertical planes at three downstream positions. The neutral gas plume resembles a Gaussian plume, while the dense gas plume takes a three-peak structure, even upstream of the cube array. It also retains high concentrations further downstream compared to the neutral gas plume. The largest concentrations are located quite far away from the centreline, outside of the cube array. The neutral gas plume is about three times higher than the dense gas plume at the first location, and retains roughly this height during the passage of the cube array. The height of the dense gas plume at the centreline almost doubles during the passage of the cube array, but with greatly reduced concentration levels. Hence, within the building structures, the difference between dense and neutral gas diminish.

### 5.3. Turbulent fluxes

In order to elucidate the impact the dense gas release has on the turbulence dynamics, the Reynolds stresses are investigated. Figure 13 shows the normalized Reynolds stress components for the dense and the neutral case. It is seen that the streamwise component is slightly overpredicted, a common problem when using LES. The shear stress and wall-normal components are very well predicted compared to experiments. From Figure 9 it was seen that there was nearly no dense gas above the cubes. When comparing Figure 13a to Figure 13c it is evident that the stresses are fairly similar above $z/h = 1$, i.e. the height of the dense gas plume. Below this height, a reduction in the wall-normal component $\langle ww \rangle$ is visible, indicating kinematic blocking similar to solid-wall behaviour. The vertical component of the Reynolds stress tensor are important for the production of shear stress, $\langle uw \rangle$, which in turn is important for production of turbulence kinetic energy. The figures indeed show that the shear stress $\langle uw \rangle$ is also reduced below the plume height. In the region $0.2 < z/h < 0.9$, the shear stress is reduced by a factor of two compared to the neutral case. Closer to the ground, i.e.below $z/h = 0.2$, the dense gas effect is less pronounced and in the immediate vicinity of the ground, the reduction in shear stress magnitude is 25%.

Further downstream, where the flow field is highly influenced by the building structures, the stresses are more similar. A reduction of turbulence kinetic energy in the dense gas case compared to the neutral case is visible (see Figure 15b) and it is also seen that the large scale anisotropy is increased close to the ground when releasing dense gas. As expected, the effect the dense gas exerts on the turbulence field is reduced as the cloud is diluted through the entrainment of air.

Vertical dispersion by means of turbulent motion can be quantified by considering the vertical scalar flux, $\langle wc \rangle$, which is seen in Figure 14. It is apparent that the vertical transport is significantly inhibited in the dense gas case, both by a reduction in magnitude and by the range over which the flux is important. This behaviour is reminiscent to that of stable background stratification [41]. The streamwise scalar flux on the other hand increases in magnitude for the dense gas case compared to the neutral case. Between the cubes, where the concentration of dense gas is lower, the dense gas scalar fluxes exhibit profiles more similar to the scalar fluxes of neutral gas.

### 5.4. Effects of stratification

The effect of stratification on turbulence is commonly characterized by the gradient Richardson number given by

$$Ri_g = \frac{N^2}{S^2}, \tag{8}$$

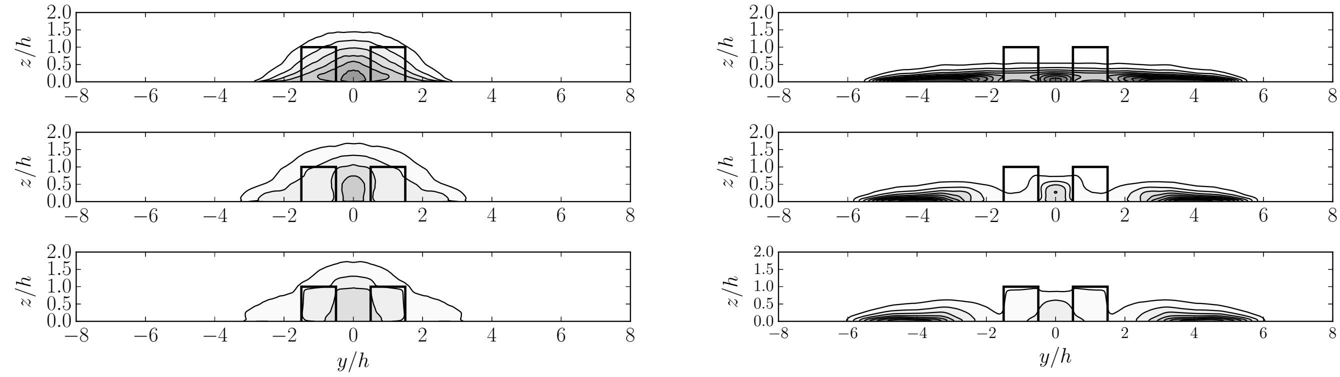

(a) Neutral gas

(b) Dense gas

Figure 12: Contours of the mean volume concentration of gas in three vertical planes. Top: $1h$ upstream of the cube array. Middle: middle of the cube array. Bottom: $1h$ downstream of the cube array. The contour spacing is 0.01.

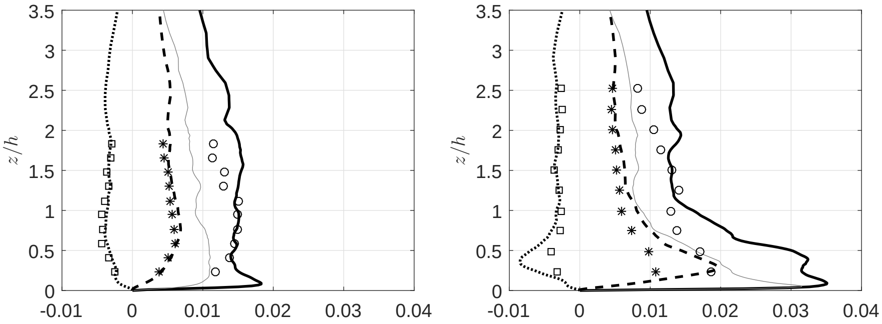

(a) Neutral case at $x/h$ = 6.88.

(b) Neutral case at $x/h$ = 9.5.

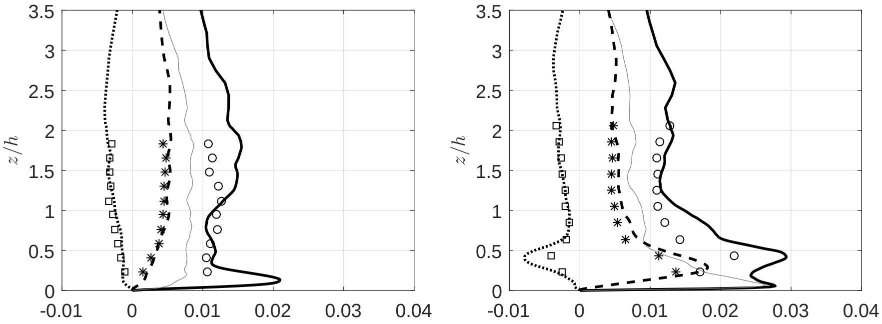

(c) Dense gas case at $x/h$ = 6.88.

(d) Dense gas case at $x/h$ = 9.5.

Figure 13: Normalized Reynolds stress components, $\langle u_i u_j \rangle / U_\infty^2$, at two different $x$-positions on the centreline. Lines show numerical results and symbols mark experimental values. $\langle uu \rangle / U_\infty^2$ (——, ∘), $\langle vv \rangle / U_\infty^2$ (——), $\langle ww \rangle / U_\infty^2$ (−−−, ∗), $\langle uw \rangle / U_\infty^2$ (⋯⋯, □).

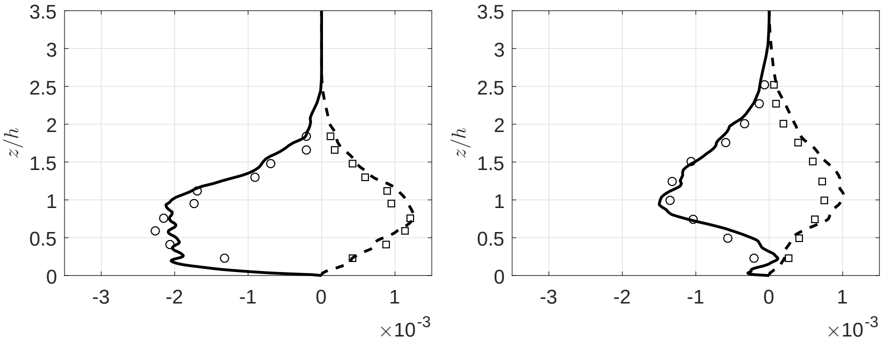

(a) Neutral case at $x/h = 6.88$.  (b) Neutral case at $x/h = 9.5$.

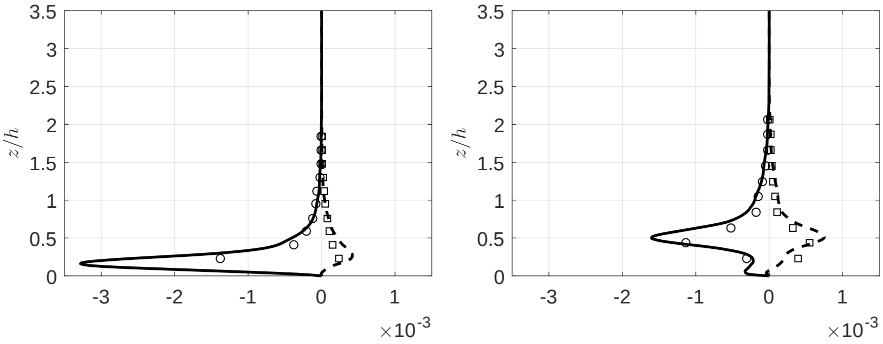

(c) Dense gas case at $x/h = 6.88$.  (d) Dense gas case at $x/h = 9.5$.

Figure 14: Normalized scalar flux components, $\langle u_i c\rangle/U_\infty$, at two different $x$-positions on the centreline. Lines show numerical results and symbols mark experimental values. $\langle uc\rangle/U_\infty$ (——, ∘), $\langle wc\rangle/U_\infty$ (– – –, □).

which represents the ratio of buoyancy to shear forcing. The Brunt–Väisälä frequency is $N^2 = -(g/\rho_{air})(\partial\rho/\partial z)$ and $S = \sqrt{2S_{ij}S_{ij}}$ is the norm of the mean strain-rate tensor. It has been shown, both theoretically [42] and experimentally [43], that flows with a gradient Richardson number less than the critical value of $\mathrm{Ri}_{g,c} = 0.25$ are dynamically unstable.The accepted range of this number varies between 0.2 to 1 and values above this tend to imply locally stable flow, in which the turbulence is significantly affected by buoyancy. It should be noted that $\mathrm{Ri}_{g,c}$ is by no means a valid criterion of turbulence extinction in itself and turbulence may survive in flows with values exceeding unity [44].

Figure 15a shows the vertical variation of the gradient Richardson number, along with the linear stability criterion, $\mathrm{Ri}_{g,c} = 0.25$, upstream of the cubes. The grey area indicates at which heights the flow might be considered stably stratified. Interestingly, this does not correspond to where the concentration of dense gas is highest, since that is also where the velocity gradient is highest. Instead, there is a region in the middle of the dense gas cloud where buoyancy seems to be dominating, thereby creating a layer of stably stratified turbulent flow. By inspection of volume data it is observed that this buoyancy dominated region extends all the way from the source to $x/h \approx 7$ in front of the cubes and to $x/h \approx 9$ outside the cube array. The former location coincides with the saddle points observed in Figure 7b, indicating that the buoyancy is dynamically important in the region where the flow field is not dominated by the presence of the cubes.

Figure 15b shows the turbulence kinetic energy for dense and neutral gas in front of the cubes. Again, the grey area indicates where the gradient Richardson number exceeds the stability criterion. Close to the ground, there is no significant difference in turbulence kinetic energy between the two cases but when entering the stable region, the energy in the dense gas case is greatly reduced. This area corresponds to where $\langle uu\rangle$ is low and, even more interestingly, it is also where $\langle wc\rangle$ start to decrease (see Figures 15c and 15d). Hence, the shear close to the ground is high enough to suppress the buoyancy effects introduced by the dense gas. Further away from the ground, however, buoyancy becomes dynamically important, leading to a reduction both in turbulence kinetic energy and of the anisotropy of the large scale turbulence. Above the dense gas cloud, the flow field is approximately the same as in the neutral case.

## 6. Concluding remarks

Large-eddy simulation of dispersion of neutral and dense gas over an array of four cubes have been performed, and results have been compared to wind-tunnel experiments. First- and second-order statistics of the velocity and concentrations have been reported and are in very good agreement with experimental results.

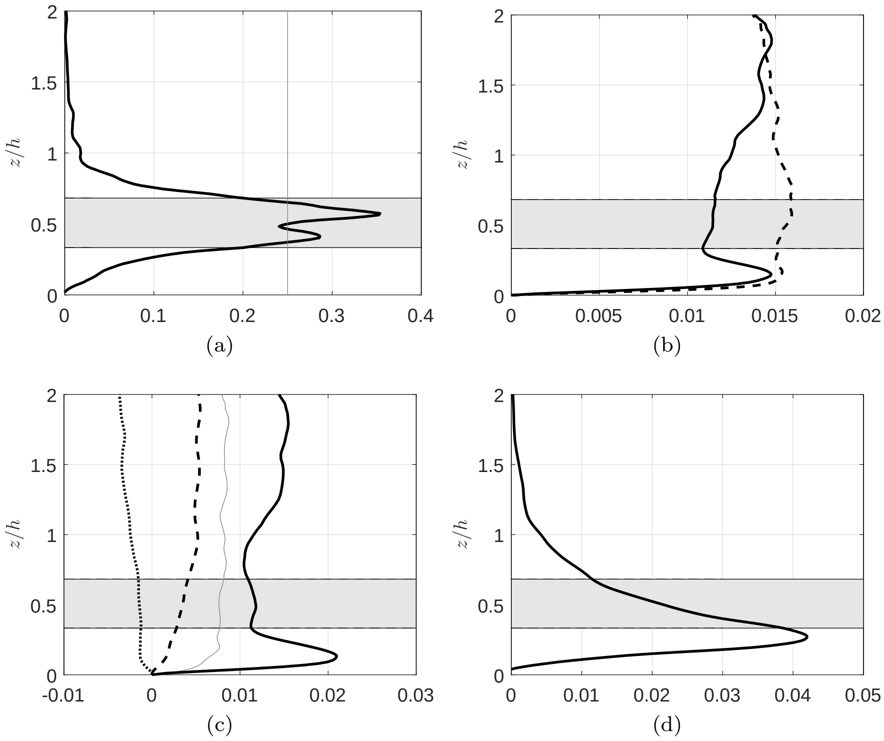

(a) (b)

(c) (d)

Figure 15: (a) Gradient Richardson number. (b) $k/U_\infty^2$, dense (——) and neutral (– – –). (c) $\langle u_i u_j \rangle / U_\infty^2$ for dense gas with lines as in Figure 13. (d) $\langle wc \rangle / U_\infty \cdot 10^{-2}$ for dense gas. All lines are taken at $x/h = 6.88$. The grey areas indicate region where the flow can be characterized as stably stratified.

Three different methods for generating an appropriate inflow boundary layer have been investigated. It is found that the combination of roughness elements and synthetic turbulence results in excellent inflow conditions for the dispersion simulations in this study.

Dense gas affects the near-source region significantly and introduces an upwind spread not seen in the neutral case. The subsequent dispersion pattern is also changed and to be able to predict this, special care needs to be taken regarding modelling of the source. The interaction between the gases and the obstacles are clearly different as well, where the dense gas seems to be more affected by the blocking of the cubes. Within the cube area, velocity and concentration fields of the neutral and dense gases are more similar.

It is seen that the root-mean-square of the scalar fluctuations, especially for the neutral gas, has the same order of magnitude as the mean scalar concentration level across the plume. This particular feature may be of significant importance when considering certain toxic chemicals where a short-duration exposure is lethal.

The dense gas reduces the vertical and spanwise turbulent momentum transport, as well as the shear stress, whereas the streamwise turbulent momentum transport is enlarged. The turbulence kinetic energy is lowered in part of the dense gas cloud and close to the ground the large-scale anisotropy is slightly enlarged compared to the neutral case. In similar manner, the vertical scalar flux is substantially lower in the dense gas case, similar to the case with a stably stratified background, while the streamwise scalar flux increases in magnitude.

The vertical scalar flux contributes to the buoyancy production of turbulence kinetic energy and it is seen that the decrease of $\langle wc \rangle$ coincide with where the gradient Richardson number exceeds the critical value of approximately 0.2. In the area where the flow may be considered to be dynamically stable, the turbulence kinetic energy is at its lowest in comparison to the neutral case. Interestingly, the stable area does not correspond to where the concentration of dense gas is highest as this is also where the velocity gradients are highest.

## Acknowledgement

This work was conducted within the European Defence Agency (EDA) project B-1097-ESM4-GP "Modelling the dispersion of toxic industrial chemicals in urban environments" (MODITIC). This research was in part supported by the computational resources at NTNU provided by NOTUR.

[1] M. Lateb, R. Meroney, M. Yataghene, H. Fellouah, F. Saleh, M. Boufadel, On the use of numerical modelling for near-field pollutant dispersion in urban environments- A review, Environmental Pollution 208 (2016) 271–283.

[2] V. Boppana, Z.-T. Xie, I. P. Castro, Large-eddy simulation of dispersion from surface sources in arrays of obstacles, Boundary-layer meteorology 135 (3) (2010) 433–454.

[3] H. Fossum, B. P. Reif, M. Tutkun, T. Gjesdal, On the use of computational fluid dynamics to investigate aerosol dispersion in an industrial environment: a case study, Boundary-layer meteorology 144 (1) (2012) 21–40.

[4] Y. Liu, G. Cui, Z. Wang, Z. Zhang, Large eddy simulation of wind field and pollutant dispersion in downtown Macao, Atmospheric environment 45 (17) (2011) 2849–2859.

[5] M. McBride, A. Reeves, M. Vanderheyden, C. Lea, X. Zhou, Use of advanced techniques to model the dispersion of chlorine in complex terrain, Process Safety and Environmental Protection 79 (2) (2001) 89–102.

[6] G. A. Perdikaris, F. Mayinger, Numerical simulation of heavy gas cloud dispersion within topographically complex terrain, Journal of loss prevention in the process industries 7 (5) (1994) 391–396.

[7] S. Sklavounos, F. Rigas, Validation of turbulence models in heavy gas dispersion over obstacles, Journal of Hazardous Materials 108 (1) (2004) 9–20.

[8] S. Tauseef, D. Rashtchian, S. Abbasi, CFD-based simulation of dense gas dispersion in presence of obstacles, Journal of Loss Prevention in the Process Industries 24 (4) (2011) 371–376.

[9] W. Coirier, D. Fricker, M. Furmanczyk, S. Kim, A computational fluid dynamics approach for urban area transport and dispersion modeling, Environmental Fluid Mechanics 5 (5) (2005) 443–479.

[10] F.-S. Lien, E. Yee, Numerical Modelling of the Turbulent Flow Developing Within and Over a 3-D Building Array, Part I: A High-Resolution Reynolds-Averaged NavierStokes Approach, Boundary-Layer Meteorology 112 (3) (2004) 427–466.

[11] F. Lien, E. Yee, H. Ji, A. Keats, K. Hsieh, Progress and challenges in the development of physically-based numerical models for prediction of flow and contaminant dispersion in the urban environment, International Journal of Computational Fluid Dynamics 20 (5) (2006) 323–337.

[12] J. L. Santiago, A. Martilli, F. Martín, CFD simulation of airflow over a regular array of cubes. Part I: Three-dimensional simulation of the flow and validation with wind-tunnel measurements, Boundary-layer meteorology 122 (3) (2007) 609–634.

[13] Z.-T. Xie, I. P. Castro, Large-eddy simulation for flow and dispersion in urban streets, Atmospheric Environment 43 (13) (2009) 2174–2185.

[14] A. Robins, P. Hayden, E. M. M. Wingstedt, MODITIC wind tunnel experiments, Tech. Rep. 2016/01483, Norwegian Defence Research Establishment (2016).

[15] S. B. Pope, Turbulent flows, Cambridge University Press, 2000.

[16] M. Lesieur, O. Métais, P. Comte, Large-eddy simulations of turbulence, Cambridge University Press, 2005.

[17] P. Sagaut, Large eddy simulation for incompressible flows: an introduction, Springer Science & Business Media, 2006.

[18] C. D. Pierce, P. Moin, Progress-variable approach for large-eddy simulation of non-premixed turbulent combustion, Journal of Fluid Mechanics 504 (2004) 73–97.

[19] F. Ham, G. Iaccarino, Energy conservation in collocated discretization schemes on unstructured meshes, Annual Research Briefs 2004 (2004) 3–14.

[20] F. Ham, K. Mattsson, G. Iaccarino, Accurate and stable finite volume operators for unstructured flow solvers, Annual Research Briefs (2006) 243–261.

[21] F. Ham, An efficient scheme for large eddy simulation of low-Ma combustion in complex configurations, Annual Research Briefs (Center for Turbulence Research, Stanford University) (2007) 41.

[22] N. Li, E. Balaras, U. Piomelli, Inflow conditions for large-eddy simulations of mixing layers, Physics of Fluids (1994-present) 12 (4) (2000) 935–938.

[23] J. Schlüter, H. Pitsch, P. Moin, Large-eddy simulation inflow conditions for coupling with Reynolds-averaged flow solvers, AIAA journal 42 (3) (2004) 478–484.

[24] P. R. Spalart, Direct simulation of a turbulent boundary layer up to $R_\theta = 1410$, Journal of fluid mechanics 187 (1988) 61–98.

[25] T. S. Lund, X. Wu, K. D. Squires, Generation of turbulent inflow data for spatially-developing boundary layer simulations, Journal of Computational Physics 140 (2) (1998) 233–258.

[26] A. Ferrante, S. Elghobashi, A robust method for generating inflow conditions for direct simulations of spatially-developing turbulent boundary layers, Journal of Computational Physics 198 (1) (2004) 372–387.

[27] J. Bonnet, D. Cole, J. Delville, M. Glauser, L. Ukeiley, Stochastic estimation and proper orthogonal decomposition: complementary techniques for identifying structure, Experiments in fluids 17 (5) (1994) 307–314.

[28] P. Druault, S. Lardeau, J.-P. Bonnet, F. Coiffet, J. Delville, E. Lamballais, J.-F. Largeau, L. Perret, Generation of three-dimensional turbulent inlet conditions for large-eddy simulation, AIAA journal 42 (3) (2004) 447–456.

[29] E. M. M. Wingstedt, M. Vartdal, A. N. Osnes, M. Tutkun, Development of LES inflow conditions for turbulent boundary layers, Tech. Rep. 2013/02420, Norwegian Defence Research Establishment (2013).

[30] H. Le, P. Moin, J. Kim, Direct numerical simulation of turbulent flow over a backward-facing step, Journal of fluid mechanics 330 (1) (1997) 349–374.

[31] M. Klein, A. Sadiki, J. Janicka, A digital filter based generation of inflow data for spatially developing direct numerical or large eddy simulations, Journal of computational Physics 186 (2) (2003) 652–665.

[32] P. Batten, U. Goldberg, S. Chakravarthy, Interfacing statistical turbulence closures with large-eddy simulation, AIAA journal 42 (3) (2004) 485–492.

[33] A. Keating, U. Piomelli, E. Balaras, H.-J. Kaltenbach, A priori and a posteriori tests of inflow conditions for large-eddy simulation, Physics of Fluids (1994-present) 16 (12) (2004) 4696–4712.

[34] L. Di Mare, M. Klein, W. Jones, J. Janicka, Synthetic turbulence inflow conditions for large-eddy simulation, Physics of Fluids (1994-present) 18 (2) (2006) 025107.

[35] N. Jarrin, S. Benhamadouche, D. Laurence, R. Prosser, A synthetic-eddy-method for generating inflow conditions for large-eddy simulations, International Journal of Heat and Fluid Flow 27 (4) (2006) 585–593.

[36] Z.-T. Xie, I. P. Castro, Efficient generation of inflow conditions for large eddy simulation of street-scale flows, Flow, turbulence and combustion 81 (3) (2008) 449–470.

[37] M. Pamies, P.-E. Weiss, E. Garnier, S. Deck, P. Sagaut, Generation of synthetic turbulent inflow data for large eddy simulation of spatially evolving wall-bounded flows, Physics of Fluids (1994-present) 21 (4) (2009) 045103.

[38] D. B. De Graaff, J. K. Eaton, Reynolds-number scaling of the flat-plate turbulent boundary layer, Journal of Fluid Mechanics 422 (2000) 319–346.

[39] B. Cabral, L. C. Leedom, Imaging vector fields using line integral convolution, in: Proceedings of the 20th annual conference on Computer graphics and interactive techniques, ACM, 1993, pp. 263–270.

[40] R. Sau, K. Mahesh, Dynamics and mixing of vortex rings in crossflow, Journal of fluid Mechanics 604 (2008) 389–409.

[41] H. E. Fossum, Computational modeling of stably stratified, turbulent shear flows, Ph.D. thesis, Mechanics Division, Department of Mathematics, University of Oslo (2015).

[42] J. W. Miles, On the stability of heterogeneous shear flows, Journal of Fluid Mechanics 10 (04) (1961) 496–508.

[43] J. Rohr, E. Itsweire, K. Helland, C. Van Atta, Growth and decay of turbulence in a stably stratified shear flow, Journal of Fluid Mechanics 195 (1988) 77–111.

[44] B. Galperin, S. Sukoriansky, P. S. Anderson, On the critical Richardson number in stably stratified turbulence, Atmospheric Science Letters 8 (3) (2007) 65–69.